Peer-reviewed version available at Materials 2018, 11, 1560; doi:10.3390/ma11091560

Article

Synthesis of Honeycomb-like Co_3O_4 Nanosheets with Excellent Supercapacitive Performance by morphological controlling derived from the alkaline source ratio

Wanli Jia, Jun Li*, Zhongjie Lu, Yongfei Juan and Yunqiang Jiang

School of Materials Engineering, Shanghai University of Engineering Science, Shanghai 201620, China; wanlian_jia@163.com (W.J.); zhongjielu@outlook.com (Z.L.)

* Correspondence: jacob_lijun@sues.edu.cn; Tel.:+86-21-6779-1198; Fax: +86-21-6779-1377

Abstract: Honeycomb-like Co_3O_4 nanosheets with high specific surface area were successfully synthesized on porous nickel foam by the facile hydrothermal method followed by an annealing treatment (300 °C), which were used as high-performance supercapacitor electrodes. The effects of mole ratio of hexamethylenetetramine (HMT) and $Co(NO_3)_2$ (1:1, 2:1, 3:1, 4:1, 5:1 and 6:1） as the reactants on morphological evolution and electrochemical performance of the electrodes were investigated in detail. X-ray diffractometry, transmission electron microscopy, X-ray photoelectron spectroscopy and scanning electron microscopy were applied to characterize the structure and morphology of the products. The electrochemical performance was measured by cyclic voltammetry (CV) and galvanostatic charge/discharge. The results indicated that phase constituents were almost unaffected with the change in mole ratio of HMT and $Co(NO_3)_2$. However, the significant morphological evolution of Co_3O_4 was observed with increasing the mole ratio, which was described as followed: the nanosheets accompanied with a large number of spherical nanoparticles→the formation of some strip-like particles due to the agglomeration of spherical nanoparticles→the formation of new nanosheets resulting from the growth of strip-like particles→the formation of coarse flower-like particles owing to the connection among the nanosheets→the nanosheets gradually covered with flower-like particles. Accompanied with the change, the specific surface area was increased firstly, and then decreased. A maximum was obtained in the HMT and $Co(NO_3)_2$ mole ratio of 4:1, which was further validated by CV and galvanostatic charge/discharge tests. The specific capacitance value was 743.00 $F \cdot g^{-1}$ at 1 $A \cdot g^{-1}$ in the galvanostatic charge/discharge test, which was apparently higher than those in the other mole ratios (139.11 $F \cdot g^{-1}$ in 1:1, 280.46 $F \cdot g^{-1}$ in 2:1, 503.29 $F \cdot g^{-1}$ in 3:1, 463.75 $F \cdot g^{-1}$ in 5:1 and 363.74 $F \cdot g^{-1}$ in 6:1). The change was also observed in the CV test with a scanning rate of 5 $mV \cdot s^{-1}$ (121.32 $F \cdot g^{-1}$ in 1:1, 217.33 $F \cdot g^{-1}$ in 2:1, 559.86 $F \cdot g^{-1}$ in 3:1, 693.56 $F \cdot g^{-1}$ in 4:1, 423.35 $F \cdot g^{-1}$ in 5:1 and 321.64 $F \cdot g^{-1}$ in 6:1). Co_3O_4 synthesized in the mole ratio of 4:1 also demonstrated an excellent cyclic performance, in which about 97% of the initial specific capacitance was remained at 1 $A \cdot g^{-1}$ for 500 cycles in the galvanostatic charge/discharge test. This excellent electrochemical performance was ascribed to high specific surface area of Co_3O_4 nanosheets that provide enough channels and space for ions transportion.

Keywords: hydrothermal method; Co_3O_4 nanosheets; mole ratio; electrochemical performance; HMT

1. Introduction

In today's world, with the rapid economic development and the growth of the global population, conventional energy is gradually depleted and pollution is worsening, new energy has become an urgent need for social development [1]. The supercapacitor between the traditional

capacitor and the battery has become a bright spot in the research of new energy sources due to its high power density, long cycle life, wide temperature operation range, durability in harsh environments, efficient cycling and low maintenance cost [2]. The electrode material is a decisive factor affecting the electrochemical performance of supercapacitors. Therefore, the investigation into the electrode material was becoming a breakthrough point in exploration of high-performance supercapacitors.

Some transition-metal oxides (such as RuO [3], MnO_2 [4], Co_3O_4 [5], V_2O_5 [6], SnO_2 [7], TiO_2 [8] and NiO [9]) have been explored as the promising electrode materials. Among them, Co_3O_4 is regarded as a favorable candidate for supercapacitors owing to its low cost, high theoretical capacity (890 $mAh.g^{-1}$)/specific capacitance (3560 $F.g^{-1}$) [10], comparatively low cost, abundant oxidation states for reversibility and good environmental affinity [11]. Co_3O_4 with different structures (zero-dimensional spherical/octahedral/cubical nanoparticles [19], one-dimensional nanoneedles/nanowires [20-21] with high aspect ratio and nanotubes/nanorods/ bundles [22-23] with low aspect ratio, two-dimensional irregularly-arranged nanosheets [24-25] and regularly-arranged nanobands [12]) have been synthesized by different methods such as thermal decomposition of solid phase [13], hydrothermal synthesis [14], chemical vapor deposition [15], sol-gel method [16], electrodeposition [17]. Comparatively speaking, hydrothermal method is especially widely used in the preparation domain of Co_3O_4 electrode materials considering its low cost, good crystal shape, high purity, easy operation, high production and uneasy reunion [18]. Feng et al. [19] investigated the effect of hydrothermal temperature (90-110 °C) on Co_3O_4 morphologies. A low temperature (90 °C) did not provide the enough driving force for Co_3O_4 recrystallization. However, Co_3O_4 microspheres presented the conglutinating trend with the temperature raised to 105 °C. The optimum hydrothermal temperature was confirmed as 100 °C, at which the specific capacitance of prepared Co_3O_4 microspheres was 850, 780, 700, 630 $F{\cdot}g^{-1}$ at current densities of 1, 2, 4, 8 $A{\cdot}g^{-1}$, respectively. And after 1000 cycles, approximately 90.8% of the specific capacitance was retained at a current density of 2 $A{\cdot}g^{-1}$. Xia et al. [20] synthesized Co_3O_4 nanowires in a system consisting of 30 mmol $Co(NO_3)_2$ and 3 mmol sodium nitrate at 120 °C for 12 h, which was then annealed in flowing argon at 250 °C for 1 h. The product exhibited the specific capacitance of 599 $F{\cdot}g^{-1}$ at 2 $A{\cdot}g^{-1}$ and 439 $F{\cdot}g^{-1}$ at 40 A $\cdot g^{-1}$. Chang et al. [21] also prepared the Co_3O_4 nanowires at an cobalt glucose/$Co(NO_3)_2{\cdot}6H_2O$ mole ratio of 1:2 by the hydrothermal method, followed by the annealing treatment at 300 °C. The sample exhibited a capacitance value of 471.8 $F{\cdot}g^{-1}$ at 0.5 $A{\cdot}g^{-1}$ and a cycling stability with 94.8% capacitance retention after 1000 cycles at 2 $A{\cdot}g^{-1}$. Venkatachalam et al. [22] synthesized Co_3O_4 nanorods by the hydrothermal reaction (120 °C for 12 h) between cobalt chloride ($CoCl_2{\cdot}6H_2O$) and urea [$CO(NH_2)_2$], which were then annealed at 300 °C for 5 h. The modified Co_3O_4 electrode exhibited the specific capacitance of 655 $F{\cdot}g^{-1}$ at a current density of 0.5 $A{\cdot}g^{-1}$. Mesoporous Co_3O_4 bundles were synthesized by a hydrothermal method (180 °C for 24 h) followed by an annealed treatment (350 °C for 3 h) [23]. The specific capacitance of Co_3O_4 bundles was 357 $F{\cdot}g^{-1}$ at 2 $A{\cdot}g^{-1}$ after 500 cycles. Moreover, the mesoporous Co_3O_4 was found to maintain 85.5 % specific capacitance with an increase in the current density from 1 to 20 A $\cdot g^{-1}$. Co_3O_4 nanoflakes were successfully synthesized by a hydrothermal method (90 °C for 24 h) and then annealed (300 °C for 4 h) [24]. The charge−discharge measurement showed that the specific capacitance of these electrodes was 263 $F{\cdot}g^{-1}$ within a potential range of -0.40-0.55 V, the large capacity of Co_3O_4 flakes retained 89.4 % over 1,000 consecutive cycles at 3 $A{\cdot}g^{-1}$. Duan et al. [25] prepared the two-layer Co_3O_4 film on a self-assembled monolayer polystyrene (PS) spheres template by the method (100 °C for 2 h), followed by an annealing process (250 °C for 1.5 h). The average specific capacitance calculated from the CV curve was approximately 360 $F{\cdot}g^{-1}$ at a scanning rate of 10 $mV{\cdot}s^{-1}$ and the value of 454 $F{\cdot}g^{-1}$ was retained at 2 $A{\cdot}g^{-1}$ after 2500 cycles.

Present studies mainly focus on the improvement in specific capacitance of Co_3O_4 with different morphologies by regulating some affecting factors such as the hydrothermal temperature, the reactant components and their ratios. Based on this, a correlation between morphologies and affecting factors was established to obtain Co_3O_4 with a high specific capacitance. Table 1 summarizes the specific capacitance of Co_3O_4 reported in some relative references. It can be seen that the value of Co_3O_4 is in the range from 100 to 850 $F.g^{-1}$, which is far less than its theoretical value

(about 3560 $F.g^{-1}$). Therefore, there is a significant scope for the improvement in specific capacitance of Co_3O_4.

Hexamethylenetetramine (HMT) and $Co(NO_3)_2$ are the most frequently used reactants for the hydrothermal synthesis of Co_3O_4 up to now. However, few investigations into the effect of their ratio on morphological evolution of Co_3O_4 were reported, so that their optimum ratio remains unidentified precisely. In our work, HMT and $Co(NO_3)_2$ with different mole ratios (1:1, 2:1, 3:1, 4:1, 5:1 and 6:1) were used to the hydrothermal synthesis of Co_3O_4 with high specific surface area. The morphological evolution of C_3O_4 with the change in the HMT/$Co(NO_3)_2$ mole ratio was investigated in detail. Moreover, the nucleation and growth mechanisms of Co_3O_4 were revealed clearly. Combined with the measurement results of specific capacitance, the optimum mole ratio was determined finally.

Table 1. The specific capacitance of Co_3O_4 reported in some relative references

Materials	Specific capacitance	Cycle performance	References
Co_3O_4 microspheres	850 $F{\cdot}g^{-1}$/1 $A{\cdot}g^{-1}$	90.8%/1000 cycles/2 $A{\cdot}g^{-1}$	[19]
Co_3O_4 microspheres	261.1 $F{\cdot}g^{-1}$/0.5 $A{\cdot}g^{-1}$	90.2%/2000 cycles/5 $A{\cdot}g^{-1}$	[30]
Co_3O_4 octahedras	98 $F{\cdot}g^{-1}$/1 $A{\cdot}g^{-1}$	195.9%/3000 cycles/2 $A{\cdot}g^{-1}$	[26]
Co_3O_4 particulates	224.38 $F{\cdot}g^{-1}$/2.75 $A{\cdot}g^{-1}$	72.2%/1000 cycles/2.75 $A{\cdot}g^{-1}$	[31]
Co_3O_4 nanoparticles	157 $F{\cdot}g^{-1}$/0.5 $A{\cdot}g^{-1}$	100%/2500 cycles/1 $A{\cdot}g^{-1}$	[32]
Co_3O_4 nanowires	599 $F{\cdot}g^{-1}$/20 $A{\cdot}g^{-1}$	91%/7500 cycles/2 $A{\cdot}g^{-1}$	[20]
Co_3O_4 nanowires	439 $F{\cdot}g^{-1}$/40 $A{\cdot}g^{-1}$	82%/7500 cycles/10 $A{\cdot}g^{-1}$	[20]
Co_3O_4 nanowires	471.8 $F{\cdot}g^{-1}$/0.5 $A{\cdot}g^{-1}$	94.8%/1000 cycles/2 $A{\cdot}g^{-1}$	[21]
Co_3O_4 nanorods	655 $F{\cdot}g^{-1}$/0.5 $A{\cdot}g^{-1}$	82.7%/1000 cycles/3 $A{\cdot}g^{-1}$	[22]
Co_3O_4 nanorods	352 $F{\cdot}g^{-1}$/1 $A{\cdot}g^{-1}$	129.6%/500 cycles/1 $A{\cdot}g^{-1}$	[27]
Co_3O_4 flakes	263 $F{\cdot}g^{-1}$/20 $A{\cdot}g^{-1}$	89.4%/1000 cycles/3 $A{\cdot}g^{-1}$	[24]
Co_3O_4 flakes	450 $F{\cdot}g^{-1}$/1 $A{\cdot}g^{-1}$	92%/5000 cycles/1$A{\cdot}g^{-1}$	[28]
Co_3O_4 films	325 $F{\cdot}g^{-1}$/2 $A{\cdot}g^{-1}$	139.69%/2500 cycles/2 $A{\cdot}g^{-1}$	[23]
Co_3O_4 nanoplates	231 $F{\cdot}g^{-1}$/1 $A{\cdot}g^{-1}$	97%/2000 cycles/2 $A{\cdot}g^{-1}$	[29]

2. Materials and Methods

2.1. Synthesis of Co_3O_4 nanosheet on nickel foam

All the reagents used in the experiments were analytical grade and without further purification. The nickel foam (2.5×3.5) was selected as the electrode substrate (Shanxi Powder Source Battery Materials Co.,Ltd., Taiyuan, China) and cleaned by 3 M HCl solution for 30 min to remove the NiO layer surface, and then washed with deionized water and ethanol for several times in an ultrasonic bath. After that, the samples were dried at 60 °C and weighted using an electronic balance (0.01 mg, Sartorius SQP, Beijing, China). 2 mmol $Co(NO_3)_2$ was added into a mixed solvent consisting of deionized water (20 ml) and absolute ethanol (10 ml) under magnetic stirring and then different

moles of hexamethylenetetramine (HMT) (2 mmol, 4 mmol, 6 mmol, 8 mmol, 10 mmol and 12 mmol) were added into the solution, respectively. Namely, the solutions with six HMT/$Co(NO_3)_2$ mole ratios were prepared (1:1, 2:1, 3:1, 4:1, 5:1 and 6:1). The pink solutions were then transferred into six 50 ml Teflon-liner stainless steel autoclaves (shown in Figure 1), and six pieces of nickel foam were immersed into the solutions. The autoclaves were sealed and maintained at 90 °C for 12 h, and then cooled to room temperature. The obtained samples were rinsed for several times with deionized water, dried at 60 °C for 2 h. Then the samples were annealed to obtain Co_3O_4 nanosheets for 2 h at 300 °C in air with the heating rate of 2 °C·min^{-1} and weighted again. The difference between the two weights was the amount of active substances. Six samples prepared at different mole ratios were labelled as Sample A(1:1), B(2:1), C(3:1), D(4:1), E(5:1) and F(6:1).

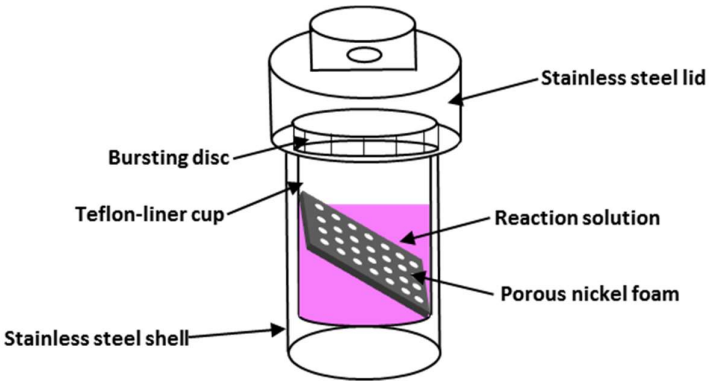

Figure 1. Schematic illustration of the Teflon-liner stainless steel autoclave.

2.2. Materials characterization

The evolution in phase constituent of the samples before and after annealing was identified by an X-ray diffractometer (XRD; D2-PHASER Bruker, Karlsruhe, Germany) using Cu Kα radiation (γ=0.1540560 nm). The elemental compositions and chemical states of the Co_3O_4 precursors and their sintered products were further determined by an X-ray photoelectron spectrometer (XPS; ESCALAB 250Xi, Thermo Fisher Scientific, Massachusetts, America). Morphologies of the annealed-samples were observed by a field-emission scanning electron microscope (FESEM; S-4800, Hitachi, Tokyo, Japan). Information about crystal structure was identified by a transmission electron microscope (TEM; JEM-2100F, JEOL, Tokyo, Japan).

2.3. Electrochemical performance

Electrochemical performance of the Co_3O_4 electrodes was measured by cyclic voltammetry (CV) and galvanostatic charge-discharge tests on a CHI 6082D (CH Instrument Ins, Shanghai, China). A 2 M KOH aqueous was used as the supporting electrolyte. A there-electrode system was applied. The nickel foam piece covered with Co_3O_4 was used as the working electrode. The graphite sheet and the saturated calomel electrode (SCE) were selected as the counter electrode and the reference electrode, respectively. The CV scannings were recorded from -0.2 to 0.6 V (vs. SCE) at different scanning rates of 5 mV·s^{-1} to 100 mV·s^{-1}, cycling stability of the Co_3O_4 electrodes was evaluated by CV for 500 cycles at 50 mV·s^{-1}. Galvanostatic charge/discharge tests were performed at different constant current densities (1, 2, 4, 6, 8, 10 A·g^{-1}).

3. Results and discussion.

3.1. XRD Results

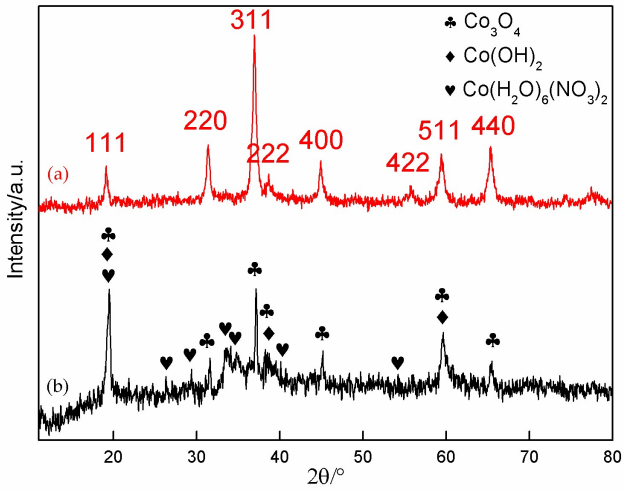

Figure 2. XRD patterns of sample D: **(a)** before the annealing; **(b)** after the annealing.

Figure 2 indicates the XRD patterns of the synthesized product in the HMT/$Co(NO_3)_2$ mole ratio of 4:1 before and after the annealing. A large number of diffraction peaks with different intensities can be observed in the XRD pattern of initial product. The indexed result shows that the product is mainly composed of $Co(OH)_2$ (JCPDS01-074-1057) and Co_3O_4 (JCPDS01-076-1802). Moreover, traces of the reactants ($Co(NO_3)_2 \cdot 6H_2O$, JCPDS01-071-0726) are found in the product. $Co(OH)_2$ is synthesized by the hydrothermal reaction as described in the following steps [25, 33]:

$$C_6H_{12}N_4 + 6H_2O \rightarrow 6HCHO + 4NH_3 \quad (1)$$

$$[Co(H_2O)_6]^{2+} + 6NH_3 \rightarrow [Co(NH_3)_6]^{2+}6H_2O \quad (2)$$

$$NH_3 + H_2O \leftrightarrow NH_4^+ + OH^- \quad (3)$$

$$[Co(NH_3)_6]^{2+} + 2OH^- \rightarrow Co(OH)_2 \downarrow + 6NH_3 \quad (4)$$

In the process of hydrothermal reaction, HMT was heated to decompose into ammonia and formaldehydethe. According to the electronic theory of acid and alkali, the alkalinity of ammonia is stronger than H_2O, it will replace H_2O in $[Co(H_2O)_6]^{2+}$ to form mental complexes with an octahedral structure. Co^{2+} and the NH_3 ligand are located at the octahedral center and the six vertex positions, respectively. Meanwhile, excessive ammonia can increase the OH^- concentration in the solution. As a result, the complex $[Co(NH_3)_6]^{2+}$ would react with OH^- to generate $Co(OH)_2$ with higher stability. Due to the remaining oxygen in Teflon-liner stainless steel autoclaves, a portion of $Co(OH)_2$ products were further oxidized to Co_3O_4 by the following reaction at high temperature.

$$6Co(OH)_2 + O_2 \rightarrow 2Co_3O_4 + 6H_2O \quad (5)$$

After the product was annealed for 2 hours at 300 °C, the XRD pattern presents the significant change. The pattern becomes smoother and the diffraction peaks related to $Co(NO_3)_2 \cdot 6H_2O$ almost disappear, indicating that $Co(NO_3)_2 \cdot 6H_2O$ had been completely decomposed into Co_3O_4 and some gases (NO_2 and O_2) by the following reaction:

$$3Co(NO_3)_2 \rightarrow Co_3O_4 + 6NO_2 + O_2 \quad (6)$$

Based on the changes in intensity of three strong peaks related to Co_3O_4 and $Co(OH)_2$, it can be concluded that the content of $Co(OH)_2$ is significantly reduced after the annealing due to its conversion into Co_3O_4 at high temperature. The reaction is followed [29]:

$$6Co(OH)_2 + O_2 \rightarrow 2Co_3O_4 + 6H_2O \quad (7)$$

Since main diffraction peaks related to $Co(OH)_2$ almost coincide with those related to Co_3O_4, it is very difficult to identify whether $Co(OH)_2$ is completely oxidized to Co_3O_4. However, the changes

in intensity of diffraction peaks related to $Co(OH)_2$ and Co_3O_4 prove that the rest of $Co(OH)_2$ has been reduced greatly (even removed completely) in the product after the annealing. Table 2 and Table 3 show the changes in three strong peaks of $Co(OH)_2$ and Co_3O_4. The intensities of three strong peaks of $Co(OH)_2$ are decreased obviously after the annealing, when compared with those in the initial product. It indicates that the content of $Co(OH)_2$ is remarkable reduced. The three strong peaks are also related to Co_3O_4, so they still have comparatively high intensities after the annealing. On the contrary, the intensity of the strongest diffraction peak of Co_3O_4 is enhanced from 76.94% to 98.68% after the annealing, meaning that the majority of $Co(OH)_2$ has reacted with oxygen. Figure 3 indicates the XRD patterns of six annealed samples prepared in different HMT/$Co(NO_3)_2$ mole ratios (A: 1:1, B: 2:1, C: 3:1, D: 4:1, E: 5:1, F: 6:1). The mole ratio almost has no effect on phase constituents of the samples.

Table 2. Three strong peaks associated with $Co(OH)_2$ (JCPDS01-074-1057).

Diffraction peaks	$Co(OH)_2$ (JCPDS01-074-1057)		Before the annealing		After the annealing	
	d (nm)	Intensity (%)	d (nm)	Intensity (%)	d (nm)	Intensity (%)
I	4.64	100.00	4.64	81.17	4.64	55.98
II	2.36	70.00	2.36	73.06	2.36	50.73
III	1.77	51.50	1.78	74.28	1.77	44.64

Table 3. Three strong peaks associated with Co_3O_4 (JCPDS01-076-1802).

Diffraction peaks	Co_3O_4 (JCPDS01-076-1802)		Before the annealing		After the annealing	
	d (nm)	Intensity (%)	d (nm)	Intensity (%)	d (nm)	Intensity (%)
I	2.43	100.00	2.42	76.94	2.44	98.68
II	1.43	36.00	1.43	77.01	1.43	62.95
III	2.85	32.00	2.83	74.21	2.85	62.90

TEM was applied to acquire more precise structure information of the annealed product prepared in the HMT/$Co(NO_3)_2$ mole ratio of 4:1. The morphology of the product is shown in Figure 4(a). A large number of equiaxed or near-equiaxed particles with smooth edges cluster together, among which numerous interfaces can be clearly observed. Besides a large particle with a size of about 80 nm, the sizes of the rest are located at the range of about 5~30 nm. It is worth noting that the contrast in different zones of those particles is approximately similar. Based on the formation mechanism of the mass thickness contrast, it can be concluded that nanosheets with similar thickness are successfully synthesized. The lattice fringes are shown in a HRTEM image (Figure 4(b)). The plane distances in different zones were calculated to be 0.242, 0.286 and 0.468 nm for the nanosheets, which match well with the (311), (220) and (111) planes of Co_3O_4. No lattice fringes related to Co(OH) are observed, which further confirms that $Co(OH)_2$ is completely oxidized to Co_3O_4. Figure 4(c) presents the selected area electron

diffraction pattern (SEAD) of the nanosheets. Five concentric diffraction rings from the center can be observed. It has been demarcated with the Co_3O_4 interplanar crystal (111), (220), (311), (422) and (440), which are completely consistent with the XRD result.

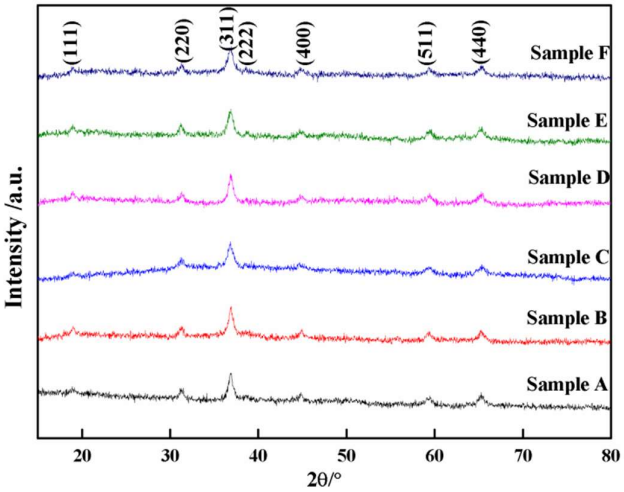

Figure 3. XRD patterns of six annealed samples prepared in different HMT/$Co(NO_3)_2$ mole ratios.

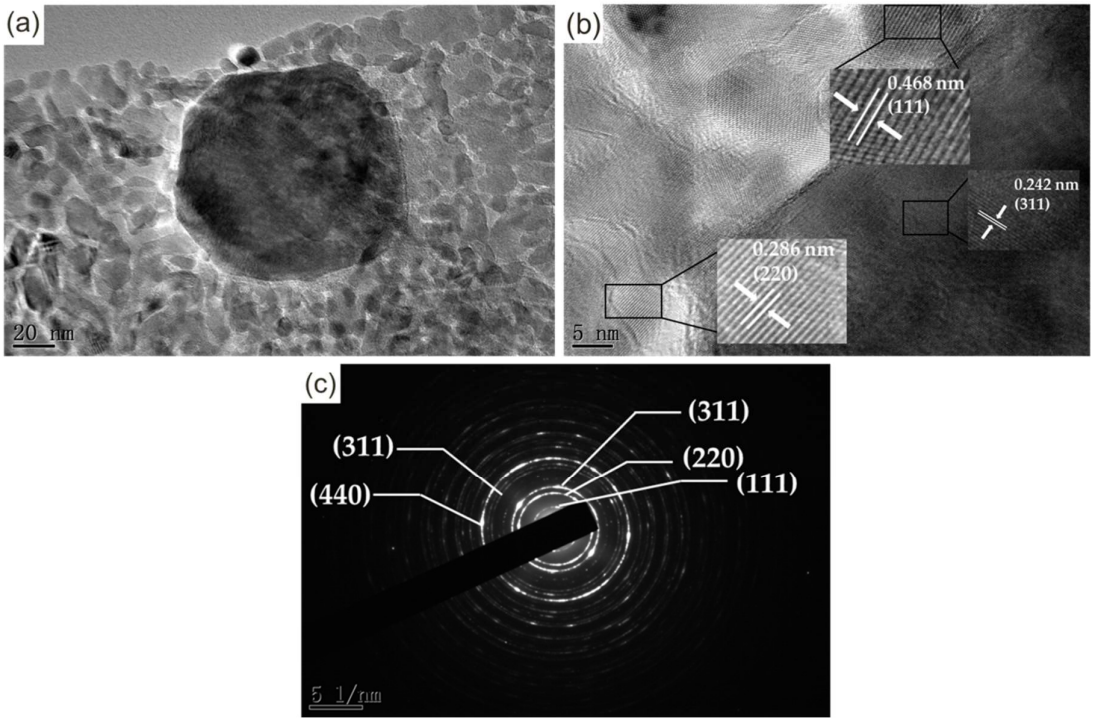

Figure 4. (a) TEM image; **(b)** Selected area electron diffraction (SEAD); and **(c)** HRTEM image of the annealed product prepared in the HMT/$Co(NO_3)_2$ mole ratio of 4:1.

Chemical compositions of Sample D were further analyzed by XPS (shown in Figure 5(a-b). The spectroscopic spin orbit of Co 2p can be split into $2p_{1/2}$ and $2p_{3/2}$, which contain the same chemical information. There are obvious differences between the two XPS spectra before and after the annealing. According to the XPS binding energy manual, Co $2p_{1/2}$ and $2p_{2/3}$ can be fitted into three pairs (Figure 5(a)) for the product before the annealing. The Co $2p_{3/2}$ peaks with

binding energies of 786.8, 781.0 and 780.1 eV and the Co $2p_{1/2}$ peaks with binding energies of 803.05, 798.0 and 795.9 eV can be allocated to $Co(NO_3)_2$, $Co(OH)_2$ and Co_3O_4, respectively. Only two peaks located at 794.6 and 780.1 eV are retained, the other small peaks disappear completely after the annealing (Figure 5(b)). The two peaks coincide with those related to Co_3O_4. It demonstrates that intermediate product ($Co(OH)_2$) and residual reactant ($Co(NO_3)_2$) are completely converted into Co_3O_4 after the annealing.

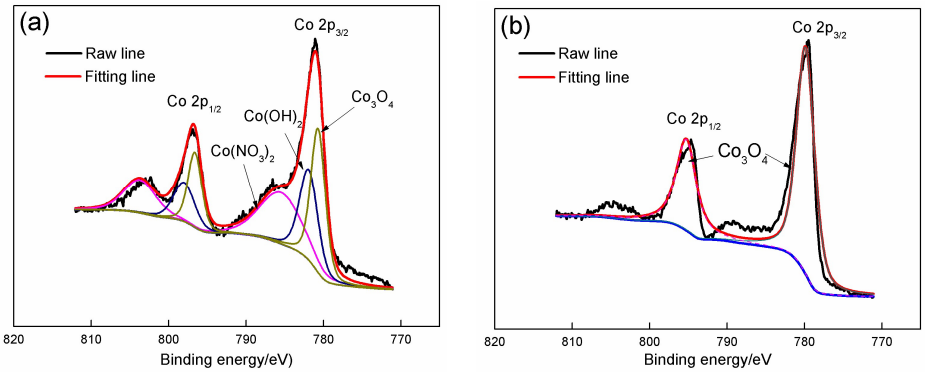

Figure 5. High resolution XPS spectra of Co 2p in sample D: (a) before the annealing; (b) after the annealing.

3.2 Morphological Characterization of Co_3O_4

SEM was used to observe the morphological evolution of the samples (shown in Figure 6(a-f)). The nickel foam is made up of a large number of three-dimensional skeletons (Figure 6(a)), among which many holes can be clearly observed. After the hydrothermal reaction, the initial surface has been completely covered with a thin layer of honeycomb-like products with loose and porous structures (Figure 6(b)). A small quantity of flower-like particles with big size protrude from the surfaces of honeycomb-like products located around the edges of nickel foam, which mainly result from the excessive growth of the products around these zones. With further increasing HMT concentration to 6 mmol and 8 mmol, the flower-like particles are corresponding increased both in size and in quantity (Figure 6(c) and (d)). The majority of the surfaces of honeycomb-like products are still uncovered. However, when the HMT concentration is enhanced to 10 mmol, the morphology of the product exhibits a significant change (Figure 6(e)). A large number of flower-like particles continue to grow and spread from the edge to the middle of nickel foam, resulting in over 70% of the surfaces of nickel foam covered by these particles. The flower-like particles are predominant in the product. The honeycomb-like particles have been completely transformed into flower-like particles at the HMT concentration of 12 mmol (Figure 6(f)). Close inspection reveals that the honeycomb-like particles possess the higher specific surface area when compared with that of the flower-like particles.

More morphological features are shown in high magnification SEM images (shown in Figure 7(a-f)). Numerous nanosheets with a thickness of about 4 nm protrude from the comparatively flat surface and connect with each other, resulting in the formation of the honeycomb-like structure (Figure 7(a)). Moreover, a large number of fine spheroidal particles with a diameter of about 100 nm are clearly observed. A high-magnification image located in the upper right corner of Figure 7(a) clearly indicates that those particles result from the excessive growth of the partial zones. When the concentration of HMT is enhanced to 4 mmol, the nanoparticles grow to about 200 nm and cluster together (Figure 7(b)). As a result, some strips of protrusions similar to nanosheets are formed (the white circle marked in the Figure 7(b)). These protrusions will grow into nanosheets with increasing the concentration of HMT (Figure 7(c)). The independently dispersed nanoparticles almost

disappear and are completely transformed into nanosheets at the HMT concentration of 0.8 mmol (Figure 7(d)). The product surface is split up into smaller scattered zones with numerous nanosheets, among which some narrow gaps are maintained. The evolution contributes to the increase in specific area of the product. However, with the further increase in concentration of HMT, nanosheets continue to grow and are interconnected to form new growth sites, which finally grow into coarse flower-like particles (Figure 7(e) and (f)). Initial honeycomb-like particles are vaguely visible and completely covered with coarse flower-like particles at the HMT concentration of 1.0 and 1.2 mmol.

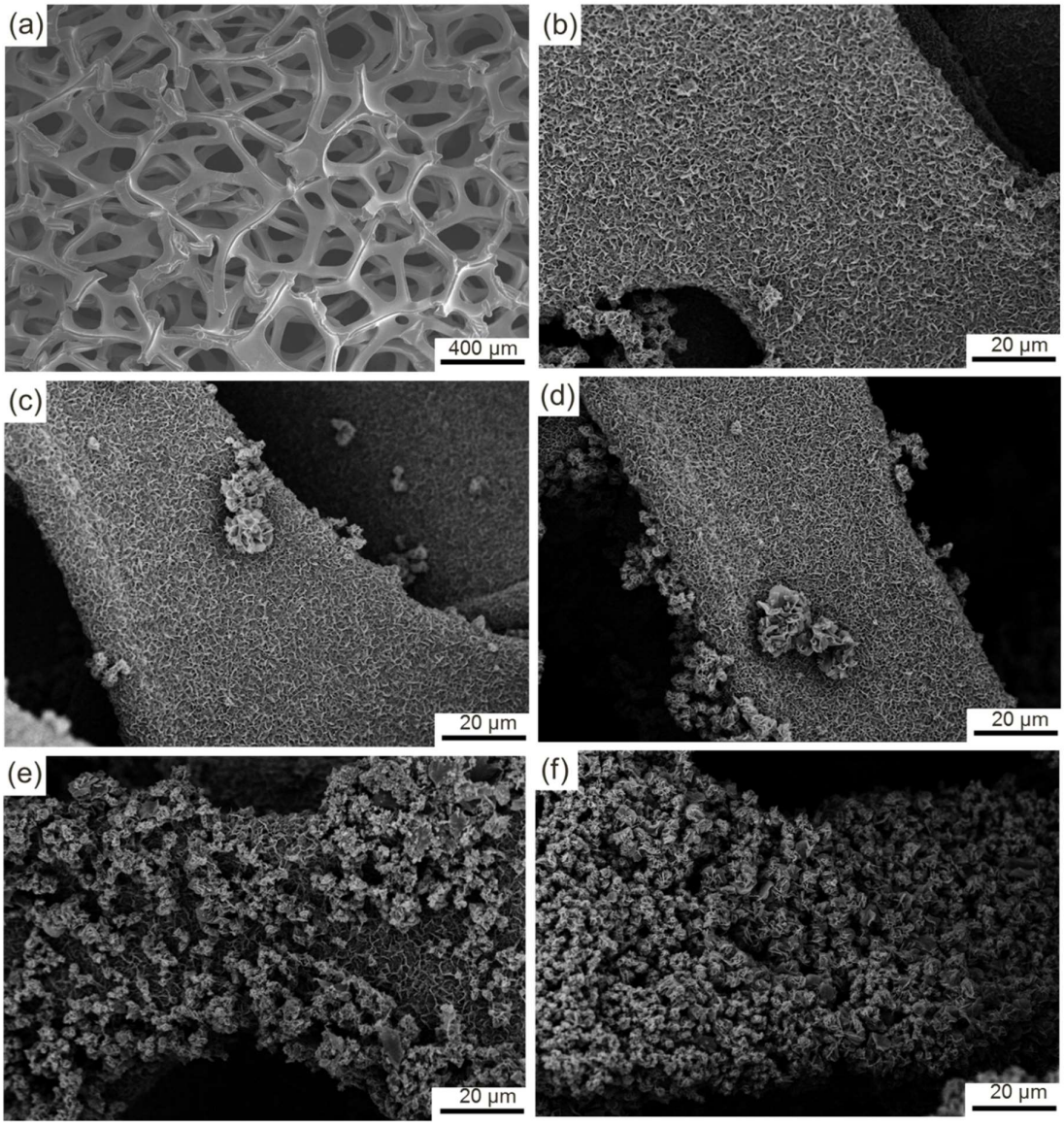

Figure 6. (a) SEM image of nickel foam; (b-f) Low magnification SEM images of samples B-F

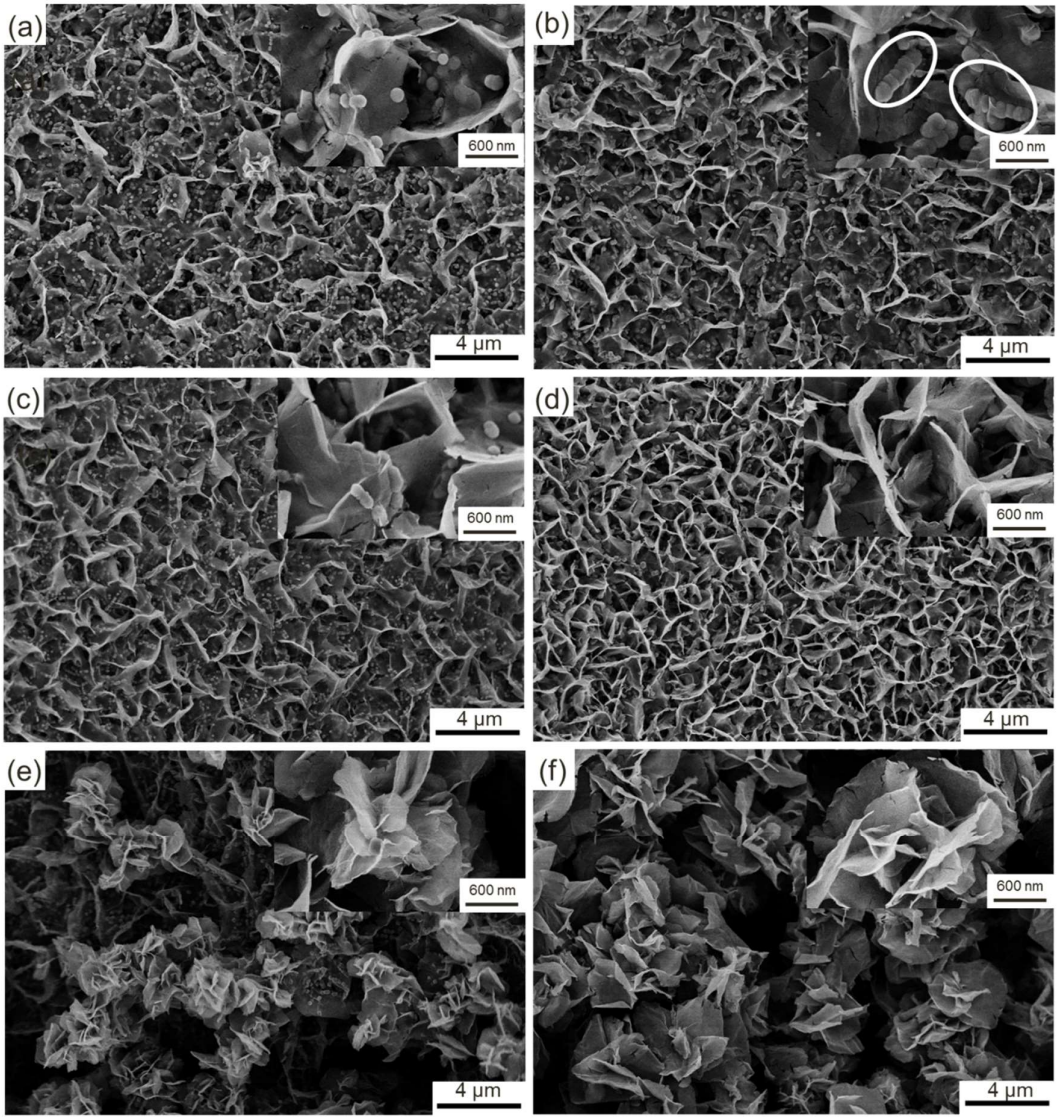

Figure 7. SEM images of the samples: (a) Sample A; (b) Sample B; (c) Sample C; (d) Sample D; (e) Sample E; (f) Sample F.

The morphological evolution can be intuitively described as follows. The fine nuclei adhering to the surface of nickel foam constantly grow omnidirectionally and are gradually connected with each other, resulting in the formation of a comparatively flat surface is formed. Along with prolonging the reaction time, the grain boundary with higher energy will grow preferentially when compared with the grain. As a result, numerous fine nanosheets grow along the grain boundaries, resulting in the formation of honeycomb-like structure. Nanosheets also present tiny changes in morphology due to the difference in concentration of reactants. The similar phenomenon also occurs at the flat zones surrounded by the nanosheets. Some local zones with a higher growth rate preferentially protrude from the product surface and grow into some fine nanoparticles. Those spherical nanoparticles will be interconnected into the long strip-like particles with more HMT added into the solution, accompanied which initial nanosheets also grow constantly. A higher concentration of HMT will hasten the growth of the long strip-like particles, resulting in the formation of sheet-like particles similar to initial nanosheets. With the increase in density of nanosheets, some new growth sites will be inevitably formed and grow into the flower-like particles. The specific area surface is increase firstly, and then reduced with the increase in HMT

concentration. The highest specific area surface should be obtained in the product prepared in the HMT/$Co(NO_3)_2$ mole ratio of 4:1.

The morphological evolution of the product is closely related to the concentration of HMT, which becomes a crucial factor affecting the growth of the product. Obviously, a high HMT concentration will offer a stronger driving force to accelerate the growth of the nuclei. According to the synthesis process of $Co(OH)_2$ described in Eqs. (1-4), HMT can sufficiently react with $Co(NO_3)_2$ to form $Co(OH)_2$ when their mole ratio is 2:1. However, that is not the case. HMT may completely consumed, but a portion of $Co(NO_3)_2$ may be remained, which should be attributed to the important intermediate product (NH_3). NH_3 originates from the reaction between HMT and H_2O, which further reacts with $[Co(H_2O)_6]^{2+}$ to form $[Co(NH_3)_6]^{2+}$. Finally, $Co(OH)_2$ is synthesized by the reaction between $[Co(NH_3)_6]^{2+}$ and OH^-. Due to the highly volatile characteristic of NH_3, a portion of NH_3 escapes from the solution, the rest can only consume a portion of added $Co(NO_3)_2$. That is to say, $Co(NO_3)_2$ may be excessive when HMT and $Co(NO_3)_2$ with a theoretical mole ratio of 2:1 are added into the solvent. Therefore, a higher mole ratio of is very essential to ensure the completely reactions between the two reactants. The evolution in morphology of the products also confirms that more $Co(OH)_2$ is synthesized with the mole ratio increased from 1:1 to 6:1.

3.3. Electrochemical characterization

Fig. 8 shows the CV results of Co_3O_4 electrodes prepared on nickel foam at various HMT/$Co(NO_3)_2$ mole ratios. The scanning potential is swept from -0.2 V to 0.8 V, and the scanning rate is changed from 5 $mV \cdot s^{-1}$ to 100 $mV \cdot s^{-1}$. It is obvious that all CV curves obtained are seriously deviate from a standard rectangle, which means that the electrodes exhibit the typical pseudocapacitance behavior. The capacitance mainly originates from the redox reactions occurring between the active substance and the electrolyte, which can be confirmed by two clear redox peaks indicated in Figure 8. When the scanning rate is set at 100 $mV \cdot s^{-1}$, two oxidation peaks are located at 0.3 V and 0.45 V, accompanied with two matching reduction peaks observed at 0.15 V and 0.28 V, respectively. With the scanning rate reduced from 100 $mV \cdot s^{-1}$ to 5 $mV \cdot s^{-1}$, the positions of the two oxidation peaks move to lower potentials, the matching reduction peaks shifts to higher potentials. The phenomenon may be attributed to the electrode reaction seriously deviating from the equilibrium state with increasing the scanning rate. The two redox reactions occurring on the electrode surface can be described as follows [34]:

$$Co_3O_4 + OH^- + H_2O \leftrightarrow 3CoOOH + e^- \quad (8)$$

$$CoOOH + OH^- \leftrightarrow CoO_2 + H_2O + e^- \quad (9)$$

The integrated area surround by CV curves is closely related to the HMT/$Co(NO_3)_2$ mole ratio. With the increase in mole ratio of HMT/$Co(NO_3)_2$ from 1:1 to 4:1 at any given scanning rate, the area presents the increasing tendency. However, the further increase in the mole ratio causes the reduction in area. The area peak is acquired in the HMT/$Co(NO_3)_2$ molar ratio of 4:1. Due to the electrode capacitance proportionate to the integrated area, it can be concluded that the capacitance can reach a maximum in the molar ratio of 4:1. The calculated results of the specific capacitance further confirm this. The specific capacitance values of Co_3O_4 can be calculated by integrating the area of the CV curves as follows [35]:

$$C_m = \frac{1}{mv(\Delta V)} \int_{V_a}^{V_c} I(V) dV \quad (10)$$

where ΔV signifies the specific capacitance (F·g-1) measured from CV tests, m is the mass of Co3O4 adhereing to nickel foam (g), ΔV denotes the potential range, V and I(V) represent the scan rate (V·s-1) and the corresponding current response, respectively.

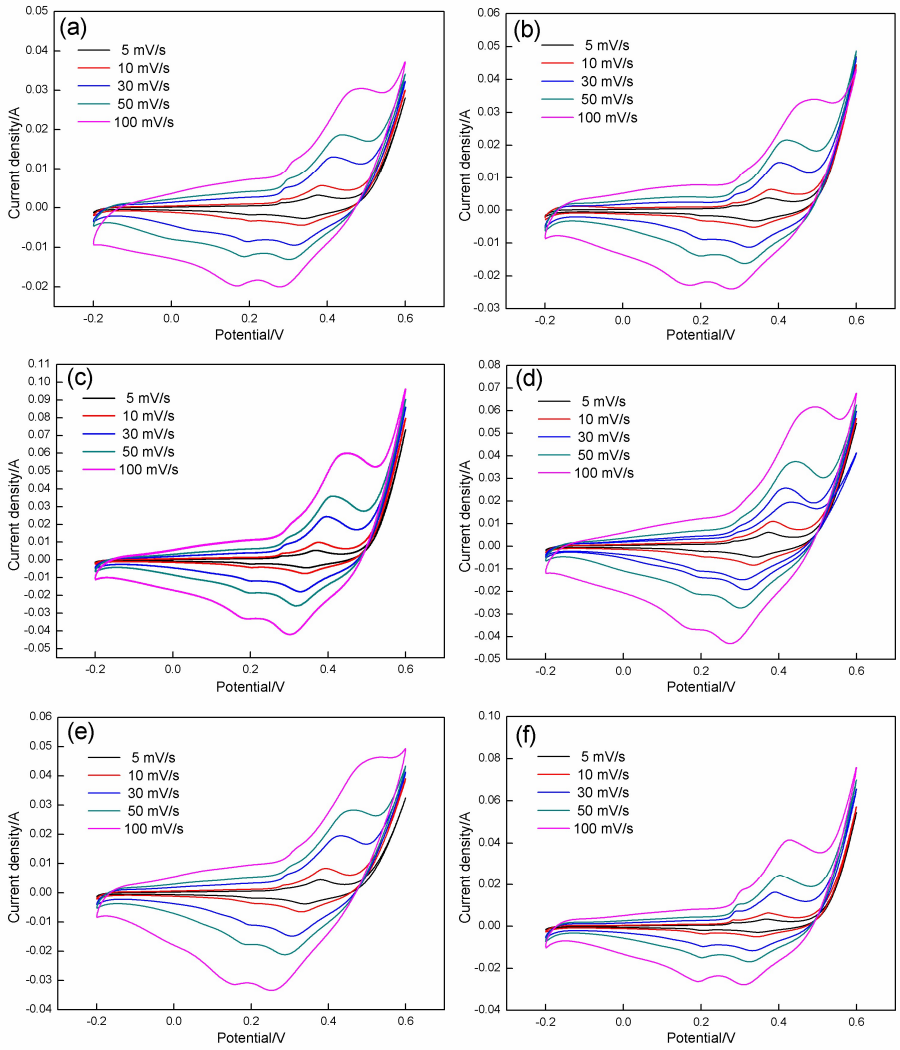

Figure 8. CV curves recorded on the samples at different scanning rates: (a) Sample A; (b) Sample B; (c) Sample C; (d) Sample D; (e) Sample E; (f) Sample F.

Based on the above equation, the specific capacitance values of six samples at various scanning rates are calculated. As shown in Table 4, sample D with the HMT/$Co(NO_3)_2$ mole ratio of 4:1 possesses the highest value (693.56 $F \cdot g^{-1}$) at a scanning rate of 5 $mV \cdot s^{-1}$, followed by sample C with the mole ratio of 3:1 (559.86 $F \cdot g^{-1}$), sample E with the mole ratio of 5:1 (423.35 $F \cdot g^{-1}$), sample F with the mole ratio of 6:1 (321.64 $F \cdot g^{-1}$), sample B with the mole ratio of 2:1 (217.33 $F \cdot g^{-1}$), sample A with the mole ratio of 1:1 (121.32$F \cdot g^{-1}$). The same tendency can be observed at the other scanning rates.

Figure 9 presents the galvanostatic charge/discharge profiles of the products synthesized in different mole ratios in the potential range of 0 to 0.45 V with different charging and discharging current densities. Those profiles are also deviated from a typical symmetrical triangular shape, and two charge/discharge platforms can be clearly observed (especially at a low current density), indicating that products present the pseudocapacitance characteristic. The charge/discharge time is heavily reliant on the mole ratio of HMT/$Co(NO_3)_2$, which is increased first and then decreased with increasing the mole ratio. The longest time period is obtained in the HMT/$Co(NO_3)_2$ mole ratio of 4:1, which means that the maximum specific capacitance is acquired at 4:1. This is well in accordance with that confirmed in CV tests. The specific capacitance of the products can be calculated according to the following equation [36]:

$$C_m = \frac{I \cdot \Delta t}{m \cdot \Delta v} \tag{11}$$

where C_m is the specific capacitance measured from galvanostatic charge/discharge curve ($F \cdot g^{-1}$), I represents the constant discharge current (A), m is the mass of Co_3O_4 (g), Δt (s) is discharge time and Δv is the potential range (V).

The result is listed in Table 5. The highest specific capacitances are also obtained in the product prepared in the HMT/$Co(NO_3)_2$ mole ratio of 4:1 at any given specific current density (743.00, 730.74, 710.93, 697.32, 680.88 and 621.21 $F \cdot g^{-1}$ at a current density of 1, 2, 4, 6, 8, and 10 $A \cdot g^{-1}$).

Table 4. Specific capacitance values of six samples at different scanning rates.

Sample	A	B	C	D	E	F
5 $mV \cdot s^{-1}$	121.32 $F \cdot g^{-1}$	217.33 $F \cdot g^{-1}$	559.86 $F \cdot g^{-1}$	693.56 $F \cdot g^{-1}$	423.35 $F \cdot g^{-1}$	321.64 $F \cdot g^{-1}$
10 $mV \cdot s^{-1}$	119.36 $F \cdot g^{-1}$	206.32 $F \cdot g^{-1}$	508.58 $F \cdot g^{-1}$	616.84 $F \cdot g^{-1}$	405.32 $F \cdot g^{-1}$	309.49 $F \cdot g^{-1}$
30 $mV \cdot s^{-1}$	107.32 $F \cdot g^{-1}$	182.09 $F \cdot g^{-1}$	416.62 $F \cdot g^{-1}$	510.40 $F \cdot g^{-1}$	386.96 $F \cdot g^{-1}$	298.76 $F \cdot g^{-1}$
50 $mV \cdot s^{-1}$	100.03 $F \cdot g^{-1}$	169.73 $F \cdot g^{-1}$	347.07 $F \cdot g^{-1}$	443.91 $F \cdot g^{-1}$	343.13 $F \cdot g^{-1}$	263.16 $F \cdot g^{-1}$
100 $mV \cdot s^{-1}$	90.32 $F \cdot g^{-1}$	153.32 $F \cdot g^{-1}$	301.01 $F \cdot g^{-1}$	354.85 $F \cdot g^{-1}$	299.16 $F \cdot g^{-1}$	214.66 $F \cdot g^{-1}$

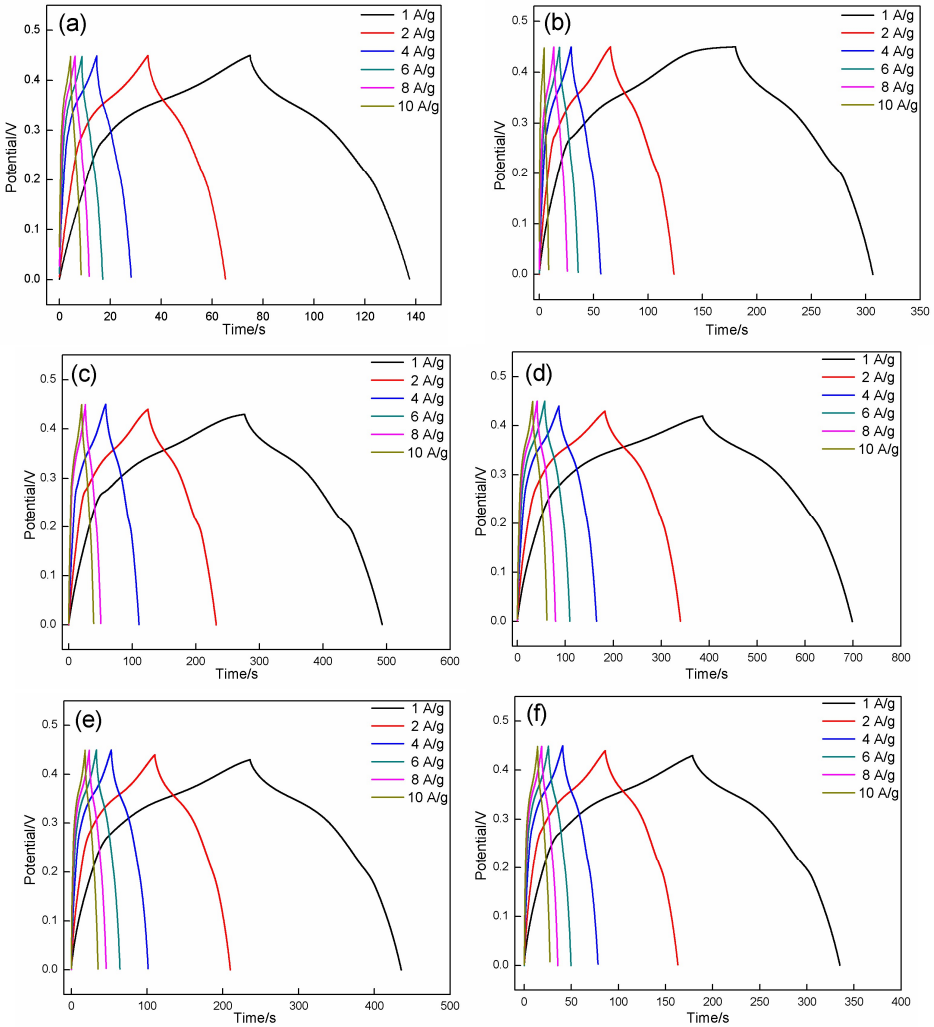

Figure 9. Galvanostatic charge/discharge curves recorded on the samples at different current densities: (a) Sample A; (b) Sample B; (c) Sample C; (d) Sample D; (e) Sample E; (f) Sample F.

Table 5. Specific capacitance values of six samples at different current density.

Sample	A	B	C	D	E	F
1 $A \cdot g^{-1}$	139.11 $F \cdot g^{-1}$	280.46 $F \cdot g^{-1}$	503.29 $F \cdot g^{-1}$	743.00 $F \cdot g^{-1}$	463.75 $F \cdot g^{-1}$	363.74 $F \cdot g^{-1}$
2 $A \cdot g^{-1}$	135.11 $F \cdot g^{-1}$	289.11 $F \cdot g^{-1}$	487.75 $F \cdot g^{-1}$	730.74 $F \cdot g^{-1}$	452.73 $F \cdot g^{-1}$	350.46 $F \cdot g^{-1}$
4 $A \cdot g^{-1}$	120.89 $F \cdot g^{-1}$	240.89 $F \cdot g^{-1}$	465.71 $F \cdot g^{-1}$	710.93 $F \cdot g^{-1}$	431.99 $F \cdot g^{-1}$	332.44 $F \cdot g^{-1}$
6 $A \cdot g^{-1}$	109.33 $F \cdot g^{-1}$	229.33 $F \cdot g^{-1}$	446.66 $F \cdot g^{-1}$	697.32 $F \cdot g^{-1}$	413.33 $F \cdot g^{-1}$	318.66 $F \cdot g^{-1}$
8 $A \cdot g^{-1}$	99.56 $F \cdot g^{-1}$	220.45 $F \cdot g^{-1}$	430.21 $F \cdot g^{-1}$	680.88 $F \cdot g^{-1}$	394.66 $F \cdot g^{-1}$	305.58 $F \cdot g^{-1}$
10 $A \cdot g^{-1}$	91.72 $F \cdot g^{-1}$	213.33 $F \cdot g^{-1}$	417.07 $F \cdot g^{-1}$	621.21 $F \cdot g^{-1}$	377.78 $F \cdot g^{-1}$	291.11 $F \cdot g^{-1}$

Figure 10 shows the specific capacitance of six samples as a function of scanning rate and current density. The specific capacitance is decreased with the increasing in scanning rate and current density. Six samples retain approximately 74.44%, 70.55%, 53.77%, 51.16%, 70.66%, 66.74% of the value obtained in 0.005 $V \cdot s^{-1}$ as the scan rate is increases from 0.005 to 0.1 $V \cdot s^{-1}$ and about 65.93%, 76.06%, 82.87%, 83.61%, 81.46%, 80.03% of the values obtained in 1 $A \cdot g^{-1}$ when the current density is increased from 1 to 10 $A \cdot g^{-1}$. Those sample also present an outstanding rate performance.

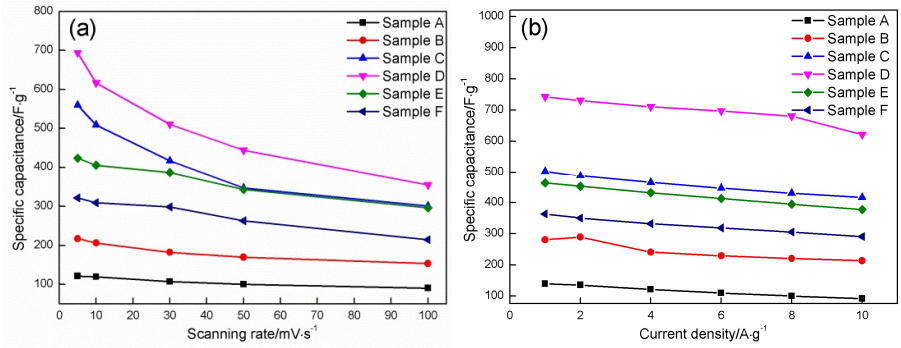

Figure 10. (a) Specific capacitance of six samples as a function of scanning rate; (b) Specific capacitance of six samples as a function of current density.

The change in specific capacitance with HMT/$Co(NO_3)_2$ mole ratio is indubitably related to the morphological evolution mentioned above, which directly determines the specific surface area. A higher specific surface area can provide more active sites for the electron exchange and shorten the transfer path of the electrons and the active ions. When the HMT/$Co(NO_3)_2$ mole ratio is 1:1, three zones with different morphologies coexist in the deposit surface, corresponding to nanosheets, flat zones surrounded by nanosheets and spherical nanoparticles uniformly distributed on the two zones. With the mole ratio of HMT/$Co(NO_3)_2$ increased to 2:1, the striped particles are formed due to the growth and interconnection among spherical nanoparticles, which possess the lower specific surface area when compared with the independently dispersed nanoparticles. However, the constant growth of nanosheets causes the increase in specific surface area. The latter plays a leading role in the change in specific surface area, resulting in the specific capacitance of the product

increased about one time（from 139.11 $F \cdot g^{-1}$ to 280.46 $F \cdot g^{-1}$ at 1 A·g-1, from 135.11 $F \cdot g^{-1}$ to 289.11 $F \cdot g^{-1}$ at 2 $A \cdot g^{-1}$, from 120.89 $F \cdot g^{-1}$ to 240.89 $F \cdot g^{-1}$ at 4 $A \cdot g^{-1}$, from 109.33 $F \cdot g^{-1}$ to 229.33 $F \cdot g^{-1}$ at 6 $A \cdot g^{-1}$, from 99.56 $F \cdot g^{-1}$ to 220.45 $F \cdot g^{-1}$ at 8 $A \cdot g^{-1}$, from 91.72 $F \cdot g^{-1}$ to 213.33 $F \cdot g^{-1}$ at 10 $A \cdot g^{-1}$）. The striped particles gradually grow into fine sheets, accompanied with constant growth of initial nanosheets in the HMT/$Co(NO_3)_2$ mole ratio of 3:1, both of which will significantly enhance the specific surface area of the product. As a result, the specific capacitance of the product synthesized in 3:1 is increased about 70%-95% when compared with that synthesized in 2:1. Tiny amounts of coarse follower-like particles with low specific surface area are formed due to the connection and growth of nanosheets, whose effect on the specific surface area of the product is negligible. When the ratio is increased to 4:1, flower-like particles produce the increasing effect on the specific area of the product due to their increase in number. However, the constant growth of nanotheets causes the corresponding increase in specific surface area, which completely eliminates the reverse effect resulting from flower-like particles. As a consequence, the specific capacitance is increased in 4:1. With the mole ratio is further enhanced to 8:1, the growth of flower-like particles is predominant and almost completely cover the whole surface of the product, which shield initial nanosheets from fully contacting with the active ions. The specific capacitance is corresponding reduced.

Cycling stability of Co_3O_4 electrodes is evaluated by CV tests for 500 cycles at 50 $mV \cdot s^{-1}$ (shown in Fig.11). It is clear that the specific capacitance prepared in the HMT/$Co(NO_3)_2$ mole ratio of 4:1 is higher than those in the other mole ratios. The specific capacitance of the sample prepared in 4:1 is 474.18 $F \cdot g^{-1}$ after 500 cycles, showing a capacitance retention of 97% of the initial value (488.77 $F \cdot g^{-1}$). Only a slight degradation (about 3%) was observed, which indicats that Sample D exhibits the excellent cycling stability. However, it is worth noting that the specific capacitances of the other samples are slightly increased after 500 cycling, their capacitance retention is about 112.92% (Sample A), 117.99% (Sample B), 121.50% (Sample C), 112.10% (Sample E) and 113.88% (Sample F). The phenomenon is associated with the changes in active site participating in the electron transfer and morphology resulting from the current shock during charge/discharge. More and more active sites will be activated as the electrolyte gradually infiltrates the electrode material during charge/discharge, which improves wettability and activation process of the electrode. In addition, the active substance will be inevitably subject to the repeated current shock during cycling, resulting from which the morphology of the active substance will changed locally. For Samples A and B, the activation of active sites is predominant in the increase in specific capacitance. Due to insufficient growth of nanosheets prepared in a low HMT/$Co(NO_3)_2$ mole ratio (1:1, 2:1), nanosheet with a comparatively low height will tightly adhere to the electrode surface, which are not easy to be destroyed under the current shock. Therefore, the effect of current shock on the specific capacitance of Samples A and B is negligible. Nanosheets with a large height far protrude into the electrolyte when the HMT/$Co(NO_3)_2$ mole ratio is increased to 3:1, which may be prone to break under the current shock. Accompanied with the fracture of local nanosheets, the specific capacitance will be reduced. However, the activation of more active sites causes the increase in specific capacitance. A slight increase in specific capacitance of Sample C compared with that of Sample B is the result of integration of the two factors above. With further increasing the mole ratio to 4:1, a strong current shock may generated in Sample D with the highest specific surface area due to the frequent and violent electron transfer during charge/discharge, which may accelerate the exfoliation of the nanosheets from the electrode surface during cycling. The current shock becomes the essential factor causing the decrease in specific capacitance of the sample, when compared with the activation of active sites resulting in the increase in that. As a result, there is a slight reduction in the specific capacitance. With the HMT/$Co(NO_3)_2$ mole ratio enhanced to 6:1 and 8:1, the coarse flower-like particles covering the nanosheets may fall off under the current shock and the nsnosheets with a high specific surface area is exposed to the electrolyte, along with which the specific capacitance presents the rising tendency with the cycling number.

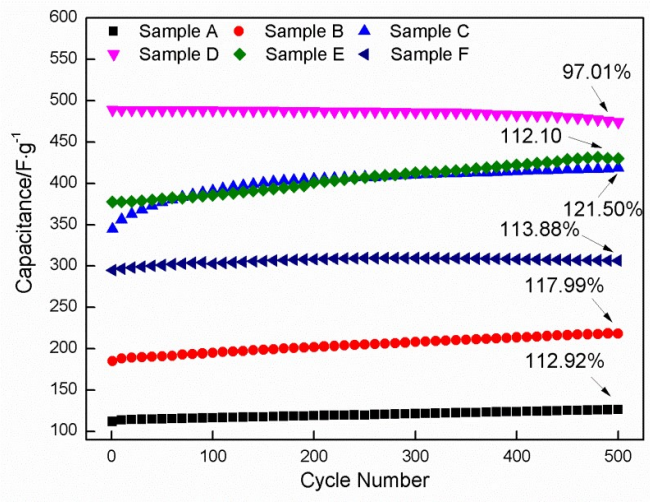

Figure 11. Cycling tests for Samples A-F at a scanning rate of 50 mV·s^{-1} up to 500 cycles.

4. Conclusions

1. Co_3O_4 nanosheets with a high specific surface area were prepared on nickel foam by hydrothermal synthesis method followed by the annealing treatment (300 °C).

2. The mole ratio of HMT and $Co(NO_3)_2 \cdot 6H_2O$ as the reactants was an essential factor determining the morphologies of Co_3O_4. With the increase in their mole ratio from 1:1 to 4:1, the nucleation and growth of nanosheets were predominant, which contributed to the enhancement in specific surface area of Co_3O_4. With the over addition of HMT (the mole ratio of HMT and $Co(NO_3)_2$ exceeded 4:1), a stronger driving force accelerated the growth and connection of nanosheets, resulting in the surface gradually covered with coarse follower-like particle with comparatively low specific surface area.

3. The specific capacitance was closely related to the morphological evolution of Co_3O_4, which was increased firstly, then decreased. A maximum value was acquired for the product synthesized in the mole ratio of HMT and $Co(NO_3)_2$ (4:1) (743.00 F·g^{-1} at 1A·g^{-1} in galvanostatic charge/discharge tests, 693.56 F·g^{-1} at 5 mV·s^{-1} in CV tests). Co_3O_4 also exhibited the excellent cyclic performance due to about 97% of initial specific capacitance remained after 500 cycling tests.

Acknowledgments: This work was financially supported by the National Natural Science Foundation of China (51471105), "Shu Guang" project of Shanghai Municipal Education Commission and Shanghai Education Development Foundation (12SG44) and "Graduate innovation" Project of Shanghai University of Engineering Science (16KY0509).

Author Contribution: Jun Li, Wanli Jia, Zhongjie Lu, Yongfei Juan and Yunqiang Jiang conceived and designed the experiments; Wanli Jia performed the experiments; Wanli Jia analyzed the data; and Jun Li and Wanli Jia wrote the paper.

Conflicts of Interest: The authors declare no conflict of interest.

References

1. Li, G.; Liu, W.L.; Wang, Z.H.; Liu, M.Q. An empirical examination of energy consumption, behavioral intention, and situational factors: evidence from Beijing. *Ann. Oper. Res.* **2017**, 255(1-2), 1-18, doi: 10.1007/s1047.
2. Parvini, Y.; Siegel, J.B; Stefanopoulou, A.G.; Vahidi, A. Supercapacitor electrical and thermal modeling, identification, and validation for a wide range of temperature and power applications. *IEEE T. Ind.*

Electron. **2016**, 63(3),1574-1585, doi: 10.1109/TIE.2015.2494868.

3. Zhang, X.; Zhao, Y.Q.; Xu, C.L. Surfactant dependent self-organization of Co_3O_4 nanowires on Ni foam for high performance supercapacitors: from nanowire microspheres to nanowire paddy fields. *Nanoscale*. **2014**, 6(7), 3638, doi: 10.1039/c3nr06734c.
4. Huang, W.X.; Li, J.; Xu, Y.H. Nucleation/Growth mechanisms and morphological evolution of porous MnO_2 coating deposited on graphite for supercapacitor. *Mater.* **2017**, 10(10), 1205, doi: 10.3390/ma10101205.
5. Vezvaie, M.; Kalisvaart, P.; Fritzsche, H.; Mitlin, D. The penetration depth of chemical reactions in a thin-film Co_3O_4 supercapacitor electrode. *J. Electrochem. Soc.* **2014**, 161(5), A798-A802, doi: 10.1149/2.081405jes.
6. Wee, G.; Soh, H.Z.; Cheah, Y.L.; Mhaisalkar, S.G. Synthesis and electrochemical properties of electrospun V_2O_5 nanofibers as supercapacitor electrodes. *J. Mater. Chem.* **2010**, 20(32), 6720-6725, doi: 10.1039/C0JM00059K.
7. Meng, X.Q.; Zhou, M.; Li, X.L.; Yao, J.Y.; Liu, F.L.; He, H.C.; Xiao, P. Synthesis of SnO_2, nanoflowers and electrochemical properties of Ni/SnO_2, nanoflowers in supercapacitor. *Electrochim. Acta.* **2013**, 109(11), 20-26, doi: 10.1016/j.electacta.2013.07.052.
8. Ambade, R.B.; Ambade, S.B.; Shrestha, N.K.; Nah, Y.C.; Han, S.H.; Lee, W.; Lee, S.H. Polythiophene infiltrated TiO nanotubes as high-performance supercapacitor electrodes. *Chem. Commun.* **2013**, 49(23), 2308-2310, doi: 10.1039/C3CC00065F.
9. Patil, U.M.; Salunkhe, R.R.; Gurav, K.V.; Lokhande, C.D. Chemically deposited nanocrystalline NiO thin films for supercapacitor application. *Appl. Surf. Sci.* **2008**, 255(5), 2603-2607, doi: 10.1016/j.apsusc.2008.07.192.
10. Meng, T.; Xu, Q.Q.; Wang, Z.H.; Li, Y.T.; Gao, Z.M.; Xing, X.Y.; Ren, T.Z. Co_3O_4 nanorods with self-assembled nanoparticles in queue for supercapacitor. *Electrochim. Acta.* **2015**, 180, 104-111, doi: 10.1016/j.electacta.2015.08.085.
11. Li, T.T.; Zhu, C.X.; Yang, X.G.; Gao, Y.H.; He, W.W.; Yue, H.W.; Zhao, H.X. Co_3O_4 nanoneedle@electroactive nickel boride membrane core/shell arrays: A novel hybrid for enhanced capacity. *Electrochim. Acta.* **2017**, 246, 226-233, doi: 10.1016/j.electacta.2017.06.054.
12. Zhao, J.w.; Zheng, Z.L.; He, X.W.; Geng, W.C. Advances in hydrothermal synthesis of Co_3O_4 nanomaterials in different dimensions. *Bull. Chem.* **2017**, 80 (12), 1093-1103, doi: 10.14159/j.cnki.0441-3776.2017.12.002.
13. Farhadi, S.; Javanmard, M.; Nadri, G. Characterization of cobalt oxide nanoparticles prepared by the thermal decomposition of $[Co(NH_3)_5(H_2O)](NO_3)_3$ complex and study of their photocatalytic activity. *Acta Chim. Slov*. **2016**, 63(2), 3, doi: 10.17344/acsi.2016.2305.
14. Yang, Y.P.; Huang, K.L.; Liu, R.S.; Wang, L.P.; Zeng, W.W.; Zhang, P.M. Shape-controlled synthesis of nanocubic Co_3O_4 by hydrothermal oxidation method. *T. Nonferr. Metal. Soc.* **2007**, 17(5), 1082-1086, doi: 10.1016/S1003-6326(07)60229-5.
15. Büyükyazi, M.; Hegemann, C.; Lehnen, T.; Tyrra, W.; Wathur, S. Molecular Co (II) and Co (III) heteroarylalkenolates as efficient precursors for chemical vapor deposition of Co_3O_4 nanowires. *Inorg. Chem*. **2014**, 53(20), 10928-36, doi: 10.1021/ic501157e.

16. Hwa, Y.; Kim, W.S.; Yu, B.C.; Hong, S.H.; Sohn, H.J. Enhancement of the cyclability of a Si anode through Co_3O_4 coating by the Sol–Gel method. *J. Phys. Chem. C.* **2013**, 117(14), 2013, doi: 10.1021/jp401333v.
17. Jagadale, A.D.; Kumbhar, V.S.; Bulakhe, R.N.; Lokhande, D.C. Influence of electrodeposition modes on the supercapacitive performance of Co_3O_4 electrodes. *Energy*, **2014**, 64(1), 234-241, doi: 10.1016/j.energy.2013.10.016.
18. Feng, Y.L.; Liu, Y.F.; Su, C.; Ji, X.H.; He, Z.K. New fluorescent pH sensor based on label-free silicon nanodots. *Sensors & Actuators B Chemical*, **2014**, 203(21), 795-801, doi: 10.1016/j.snb.2014.07.050.
19. Feng, C.; Zhang, J.F.; Deng, Y.D.; Zhong, C.; Liu, L.; Hu, W.B. One-pot fabrication of Co_3O_4, microspheres via hydrothermal method at low temperature for high capacity supercapacitor. *Mater. Sci. Eng. B.* **2015**, 199, 15-21, doi: 10.1016/j.mseb.2015.04.010.
20. Xia, X.H.; Tu, J.P.; Mai, Y.J.; Wang, X.L.; Gu, C.D.; Zhao, X.B. Self-supported hydrothermal synthesized hollow Co_3O_4 nanowire arrays with high supercapacitor capacitance. *J. Mater. Chem.* **2011**, 21(25), 9319-9325, doi: 10.1039/C1JM10946D.
21. Chang, B.B.; Gu, Z.Y.; Guo, Y.Z.; Li, Z.K.; Yang, B.C. Glucose-assisted synthesis of Co_3O_4, nanostructure with controllable morphologies from nanosheets to nanowires. *J. Alloy. Comp.* **2016**, 676, 26-36, doi: 10.1016/j.jallcom.2016.03.056.
22. Venkatachalam, V.; Alsalme, A.; Alswieleh, A.; Jayavel, R. Shape controlled synthesis of rod-like Co_3O_4, nanostructures as high-performance electrodes for supercapacitor applications. *J. Mater. Sci. Mater. Electron.* **2018**, 29(7), 6059-6067, doi: 10.1007/s10854-018-8580-8.
23. Liu, W.; Jiang, D.; Xia J.X.; Qian, J.; Wang, K.; Li, H.M. Preparation of hierarchical mesoporous Co_3O_4, bundle using [Bmim]TA as a multi-role starting material and its supercapacitor application. *Monatshefte für Chemie - Chemical Monthly*, **2014**, 145(1), 19-22, doi: 10.1007/s00706-013-0992-9.
24. Xie, L.J.; Li K.X.; Sun G.H.; Hu, Z.G.; Lv, C.X.; Wang, J.L.; Zhang, C.M. Preparation and electrochemical performance of the layered cobalt oxide (Co_3O_4) as supercapacitor electrode material. *J. Solid State Electr.* **2013**, 17(1), 55-61, doi: 10.1007/s10008-012-1856-7.
25. Duan, B.R.; Cao, Q. Hierarchically porous Co_3O_4 film prepared by hydrothermal synthesis method based on colloidal crystal template for supercapacitor application. *Electrochim. Acta.* **2012**, 64(1), 154-161, doi: 10.1016/j.electacta.2012.01.004.
26. Cao, Y.B.; Yuan, F.L.; Yao, M.S.; Bang, J.H.; Lee, J.H. A new synthetic route to hollow Co_3O_4 octahedra for supercapacitor applications. *Crystengcomm*, **2013**, 16(5), 826-833: doi: 10.1039/C3CE41840E.
27. Li, C.; Li, J.; Zhang, X.G. Preparation and properties of Co_3O_4, nanorods as supercapacitor material. *J. Appl. Electrochem.* **2009**, 39(10), 1871, doi: 10.1007/s10800-009-9891-5.
28. Xiao, A.G.; Zhou, S.B.; Zuo, C.G.; Zhuan, Y.B.; Ding, X. Controllable synthesis of mesoporous Co_3O_4 nanoflake array and its application for supercapacitor. *Mater. Res. Bull.* **2014**, 60, 674-678, doi: 10.1016/j.materresbull.2014.09.034.
29. Geng, T.; Zhang, L.; Wang H.Y. Zhang, K.Y.; Zhou, X. Facile synthesis of porous Co_3O_4 nanoplates for supercapacitor applications. *Bull. Mater. Sci.* **2015,** 38(5), 1171-1175, doi: 10.1007/s12034-015-0997-6.
30. Guo D.X.; Song, X.M.; Li, F.F.; Tan, L.C.; Ma, H.Y.; Zhang, L.L; Zhao, Y.Q. Oriented synthesis of Co_3O_4 core-shell microspheres for high-performance asymmetric supercapacitor. *Colloid. Surface. A.* **2018**, 546, 1-8, doi: 10.1016/j.colsurfa.2018.02.072.

31. Tummala, R.; Guduru, R.K.; Mohanty, P.S. Nanostructured Co_3O_4 electrodes for supercapacitor applications from plasma spray technique. *J. Power. Sources*. **2012**, 209(7), 44-51, doi: 10.1016/j.jpowsour.2012.02.071.
32. Xu, W.; Li, T.T.; Zheng, Y.Q. Porous Co_3O_4 nanoparticles derived from Co (II)-cyclohexanehexacarboxylate metal-organic framework used as supercapacitor with good cycling stability. *Rsc. Adv.* **2016**, 6(89), doi: 10.1039/C6RA17471J.
33. Ding, K.; Zhang, X.; Yang, P.; Cheng, X. Precursor-derived morphology controlling for mesoporous Co_3O_4 nanostructures towards supercapacitor application. *Crystengcomm*, **2016**, 18, 8253-8261, doi: 10.1039/C6CE01921H.
34. Wang, J.Y.; Dou, W.; Zhang X.T.; Han, W.H.; Mu, X.M.; Zhang, Y.; Zhao, X.H.; Chen, Y.X.; Yang, Z.W.; Su, Q.; Xie, E.Q.; Lan, W.; Wang, X.R. Embedded Ag quantum dots into interconnected Co_3O_4 nanosheets grown on 3D graphene networks for high stable and flexible supercapacitors. *Electrochim. Acta.* **2017**, 224, 260-268, doi: 10.1016/j.electacta.2016.12.073.
35. Barmi, A.A.M.; Aghazadeh, M.; Arhami, B.; Shiri, H.M.; Fazl, A.A.; Jangju, E. Porous cobalt hydroxide nanosheets with excellent supercapacitive behavior. *Chem. Phys. Lett.* **2012**, 541(541), 65-69, doi: 10.1016/j.cplett.2012.05.038.
36. Xu, Y.H.; Li, J.; Huang, W.X. Porous Graphene Oxide Prepared on Nickel Foam by Electrophoretic Deposition and Thermal Reduction as High-Performance Supercapacitor Electrodes. *Materials,* **2017**, 10(8), doi: 10.3390/ma10080936.